ACS OMEGA

Open Access

http://pubs.acs.org/journal/acsodf

Article

Unraveling the O_2 Reduction Reaction on 2D Monolayer $LaNiO_3$ Perovskite

Published as part of ACS Omega virtual special issue "Celebrating the 25th Anniversary of the Chemical Research Society of India".

Dikeshwar Halba and Srimanta Pakhira*

Cite This: *ACS Omega* 2024, 9, 35614−35626

Read Online

ACCESS | Metrics & More | Article Recommendations | Supporting Information

ABSTRACT: The O_2 reduction reaction (ORR) occurring at cathodes is a critical reaction in many electrochemical energy-converting devices such as fuel cells. The reaction kinematics of the ORR is generally very slow with high overpotentials and needs to be enhanced by using an efficient electrocatalyst. The highly recognized Pt-based electrocatalyst needs to be replaced with a low-cost non-noble metal-based electrocatalyst for catalyzing the ORR. We theoretically studied the structural and electronic properties of 3D bulk $LaNiO_3$ perovskite. We have cleaved the (0 0 1) surface from 3D $LaNiO_3$, which has a zero band gap (E_g), to create 2D monolayer $LaNiO_3$ computationally and studied its electronic properties. Our study demonstrates that the 2D monolayer $LaNiO_3$ is a suitable candidate for catalyzing the ORR because of its high catalytic activity with a tiny electronic band gap of 0.25 eV. We explored the ORR mechanism on the 2D monolayer $LaNiO_3$ perovskite by inspecting each intermediate. Our present findings show that the 2D monolayer $LaNiO_3$ can efficiently catalyze the ORR through a four-electron ($4e^-$) reduction reaction due to the excellent catalytic activity of its basal plane, which accords with the experimental findings. The change in Gibbs free energy (ΔG) calculations of various intermediate steps of the ORR demonstrates that all reaction steps are spontaneous and thermodynamically favorable. The 2D monolayer $LaNiO_3$ perovskite can be a potential candidate for catalyzing the ORR efficiently. This study helps to enable the development of high-activity, stable 2D perovskites for use in future solid oxide fuel cells and related applications in green energy technologies.

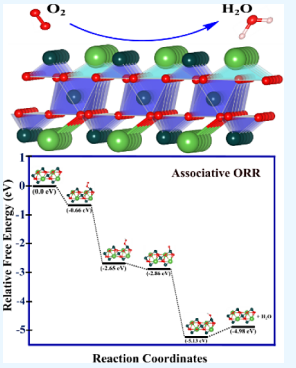

INTRODUCTION

Globally, energy requirements are at their peaks due to the increasing population. There are various renewable energy sources like solar energy, geothermal energy, wind energy, etc., from which we extract energy. However, the availability of renewable energy sources depends on weather conditions and seasonal factors, which can limit their consistent energy supply. Therefore, we rely solely on fossil fuels to meet our energy demands.[1−5] Greenhouse gases are harmful to our health due to CO_2 emissions, which take place during the consumption of fossil fuels that cause global warming by trapping heat in the atmosphere. These all have a severe impact on our environment in various ways. Hence, the development of clean, green, and renewable energy technologies or resources is highly demanded to control greenhouse gas emissions and maintain sustainable development to fulfill the energy requirements.[6,7] Fuel cells and metal−air batteries, which are ingenious energy storage and efficient energy conversion devices, have attracted many researchers because these devices can convert clean fuels, such as hydrogen, to electricity with greater efficiency while achieving high energy density.[8−10] In a variety of energy conversion and storage application devices, the oxygen reduction reaction (ORR) occurring at the cathode is an essential reaction that plays a critical role in fuel cells. The ORR mechanism involves the formation of water molecules by the reduction of oxygen molecules that involves the transfer of electrons from the electrode to the oxygen molecules. The ORR process occurs through two different mechanisms: (i) an indirect two-electron ($2e^-$) reduction path where H_2O_2 is formed or (ii) a direct four-electron ($4e^-$) reduction route where water is formed.[11−13]

The multistep ORR kinetics at the cathode are usually slow in comparison to anodic reactions, which significantly affects the performance and commercialization of electrochemical energy conversion devices in short applications.[14] An electrocatalyst plays a significant role in enhancing the efficiency and performance of fuel cells by making the ORR process faster, which is in general sluggish in nature during the O_2 reduction reaction. The volcano-type relationship is present between the

Received: April 12, 2024
Revised: June 8, 2024
Accepted: June 14, 2024
Published: August 6, 2024

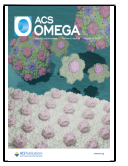

surface's electronic structure of a catalyst and its catalytic activity for the ORR.[15,16] Hence, exploring new highly active, low-cost, and stable electrocatalysts for catalyzing the ORR is vital for enhancing the efficiency of fuel cells. Advancements in preparing new highly active electrocatalytic materials are related to understanding the underlying ORR mechanisms for energy conversion devices.[17−19] Researchers have explored various catalysts; among them noble metal (Pt, Au, and Pd)-based electrocatalysts have shown remarkable performance for the ORR in fuel cells and metal−air batteries because of their excellent electrocatalytic activity and relatively low overpotential. However, due to their high cost and rarity, the precious Pt and Pt-based catalysts hinder broad applications in industries and commercialization of fuel cells made of these materials.[20−22] Therefore, the replacement of precious metal-based catalysts with alternatives having comparable or even better electrocatalytic activity is necessary for practical applications by reducing the cost. In fuel cells, oxides have demonstrated excellent catalytic activity for the ORR.[23,24] To date, various non-noble metal-based catalysts have been studied and have shown good performance for the ORR but still have some limitations within them.[24−27] The search for efficient and long-lasting catalysts for the ORR has been a major challenge, and perovskite oxides have emerged as a promising class of materials in this regard. Perovskite oxides with a crystal structure having the general formula ABO_3, where A is alkaline or rare earth metal cations (e.g., La, Ca, and Cs), B is transition metal cations (e.g., Ni, Fe, Pb, and Co), and O is an oxygen anion having a unique combination of electronic, magnetic, and structural properties make them attractive candidates for ORR catalysts.[28,29] Due to the low cost and ease of synthesis, perovskite oxides are a good alternative to noble metal-based catalysts. The segregation of alkaline earth elements such as Ba, Sr, and Ca on perovskite surfaces under an oxygen-enriched atmosphere has been widely reported. The mechanism behind oxygen activation at gas−solid interfaces is not yet fully understood, but transition metals such as Mn, Fe, Co, and Ni are the active sites where O_2 gets adsorbed. Perovskite oxide is encouraging as a Pt-free and bifunctional catalyst for fuel cells because of its Earth-abundance, high catalytic activity, and good stability under harsh conditions.[6,17,30−32]

In an alkaline medium, perovskite-based oxides are an alternative solution for efficiently catalyzing the ORR because they are highly resistive to alkaline solutions. Recently, it has been explored that the 2D monolayer $CsPbBr_3$ has shown excellent catalytic activity for the ORR that followed both associative and dissociative pathways.[6] Expanding on the promising catalytic activity of 2D monolayer $CsPbBr_3$ for the ORR, it is noteworthy to explore lanthanum nickelate ($LaNiO_3$) as another intriguing candidate in the realm of electrocatalysis. $LaNiO_3$ has gained considerable attention due to its unique electronic and magnetic properties. $LaNiO_3$ is a promising candidate for a range of applications such as catalysis due to its good conductivity and magnetic behavior. It has been reported that tuning its properties is possible via the substitution of anions and cations, e.g., adding Fe and Mg to the B-site of Ni makes $LaNiO_3$ more catalytically active.[15,33] A few studies showed that perovskite oxide with diverse compositions having better catalytic activity can be prepared by replacing the A-site and B-site with other metal ions.[34,35] Recently, it has been demonstrated that the substitution of Fe in a Co-based perovskite has shown excellent catalytic performance in an alkaline electrolyte toward the ORR.[27,36] The bifunctional catalytic activity of the most promising candidate, perovskite-based $LaNiO_3$, is efficient and comparable to those of other best-performing precious metals. Very recently, Shao-Horn et al. experimentally proved that the e_g electron number of transition metal cations is an important parameter that influences the performance of ORR activity.[27,37] The $LaNiO_3$ perovskite with Ni centers having a valency state of 3+ and moderate e_g electron occupation ($e_g \approx 1$) promotes the efficient ORR with a $4e^-$ transfer pathway. Additionally, the splitting of e_g orbitals is effective in tuning the catalytic performance of $LaNiO_3$ under the action of epitaxial strain due to changes in the electronic structure. Those compounds have exhibited higher activity whose 3d transition metal cations had only one electron in their e_g orbital.[16] Unfortunately, there is no theoretical and computational study to explain the experimental observations.

In this article, we have introduced a highly efficient ORR catalyst using a Pt-free 2D material computationally. Using the first principles-based quantum mechanical density functional theory (DFT) method, we have proposed a 2D monolayer $LaNiO_3$ perovskite material as a potential cathodic material for the ORR. At first, the equilibrium structure and electronic properties of the 3D bulk structure of $LaNiO_3$ have been studied by generating crystal structures using theoretical methods. The 3D $LaNiO_3$ material lacks the necessary high surface area for an efficient O_2 reduction reaction. To address this issue, we cleaved a (0 0 1) surface from the 3D bulk structure of the $LaNiO_3$ perovskite material as shown in Figure 1a and computationally designed a 2D monolayer $LaNiO_3$ slab

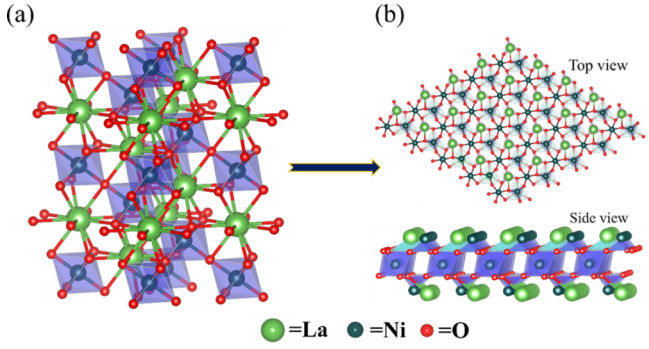

Figure 1. (a) Equilibrium geometry of the 3D bulk structure of $LaNiO_3$ and (b) top and side view of the equilibrium structure of 2D monolayer $LaNiO_3$.

structure as depicted in Figure 1b. We have selected the (0 0 1) surface because in the perovskite structure such surfaces are generally the most stable, and the atoms which drive the ORR catalytic activity are the redox-active transition metals.[15,27] We performed structural optimization and electronic property calculations of the 2D monolayer $LaNiO_3$ system. Our electronic property calculation reveals that the 3D $LaNiO_3$ is a metallic conductor with a zero band gap. But in comparison to 3D $LaNiO_3$, 2D monolayer $LaNiO_3$ has an excellent catalytic property due to its highly active exposed surface area, indicating its promising potential as an effective ORR catalyst. Furthermore, our study investigates various reaction intermediates involved on the surface of 2D monolayer $LaNiO_3$ to study the ORR process. We utilized a 2D monolayer slab configuration of the $LaNiO_3$ perovskite to thoroughly investigate each reaction step involved in the ORR mechanism,

https://doi.org/10.1021/acsomega.4c03544
ACS Omega 2024, 9, 35614−35626

considering the standard hydrogen electrode (SHE) or computational hydrogen electrode (CHE) model. We explored the ORR mechanism on the surfaces of the 2D monolayer $LaNiO_3$ perovskite to determine its catalytic activity and to explain the experimental observations.

Our research reveals that all the active sites on the surface of 2D monolayer $LaNiO_3$ exhibit strong energetics and thermodynamic favorability, establishing it as a highly promising electrocatalytic material toward the ORR. The outstanding performance of 2D monolayer $LaNiO_3$ demonstrates the exciting possibilities of designing novel electrocatalytic materials with high efficiency and stability and underscores the potential of 2D perovskite oxide-type catalysts to drive progress in clean renewable energy research.

METHODS AND COMPUTATIONAL DETAILS

All the calculations were performed by using the Vienna *Ab initio* Simulation package (VASP).[38,39] The equilibrium structure, geometry, and electronic properties of both the 3D crystal structure of $LaNiO_3$ and 2D monolayer of $LaNiO_3$ perovskite materials were computed by utilizing the projector augmented wave (PAW) approach with pseudopotentials.[40,41] In DFT, the electronic structure and total energy of the system were calculated by solving the Kohn−Sham equations, which are a set of self-consistent equations that describe the behavior of noninteracting electrons in an effective potential. The effective potential is obtained by subtracting the exchange-correlation energy functional from the external potential. The calculations involved the application of the Perdew−Burke−Ernzerhof (PBE)[42] form of generalized gradient approximation (GGA) to describe the exchange and correlation effects. A simple formulation of a GGA method for both the exchange and correlation energies of electrons was developed by Perdew, Burke, and Ernzerhof (PBE), i.e., this method includes both PBE exchange and PBE correlation parameters during computations.[42,43] To account for weak van der Waals (vdW) interactions in the systems, Grimme's semiempirical third-order dispersion correction parameters (Grimme's D3) were included in the DFT computation.[43] We employed spin-polarized calculations using periodic hybrid DFT-D (i.e., PBE-D3) method to determine the equilibrium structures and investigate the electronic properties of the studied system. In our study, the pseudopotential basis sets employed for La, Ni, and O atoms were PAW_PBE La_GW, PAW_PBE Ni_GW, and PAW_PBE O_GW, respectively, and a plane-wave cutoff energy of 450 eV was provided. A $1 \times 1 \times 1$ Monkhorst−Pack[44] k-point grid with a Gaussian smearing of 0.05 eV was used for the PBE-D3 calculations of the $LaNiO_3$ slab, and the convergence energy was set to 1×10^{-5} eV. To calculate and plot the total density of states (DOS), the atomic orbitals of La, Ni, and O atoms were employed. A 2D vacuum slab was utilized to consider the electrostatic potential of the 2D $LaNiO_3$ material. In our calculation, we have created a vacuum slab of 2D monolayer $LaNiO_3$ for studying the structural and electronic properties of the studied systems. The vacuum region was employed to avoid periodicity along the z-direction. A 15 Å vacuum region was created perpendicular to the 2D monolayer $LaNiO_3$ slab to avoid spurious interactions between the repeated layers. We employed the visualization code VESTA to generate visual representations and conduct the crystal structure analysis of the $LaNiO_3$ perovskite 2D slab.[45,46]

ORR Mechanisms. To create an effective catalyst, which is essential for renewable energy converting sources, it is crucial to understand the ORR mechanism in detail. The ORR of a fuel cell, where electrons from the anode interact with protons and oxygen to produce water at the cathode, determines its efficiency and performance. A direct four-electron ($4e^-$) transfer reaction pathway and an indirect two-electron ($2e^-$) transfer reaction pathway are the two possible directions in which the ORR may occur in acidic solutions. The more efficient direct $4e^-$ reduction path includes the adsorption of the O_2 molecule and subsequent splitting into activated oxygen atoms on the surface of the catalyst. At the cathode, the activated oxygen atoms interact with electrons and protons to produce water.[47−49] On the other hand, the indirect $2e^-$ reduction pathway involves the formation of hydrogen peroxide (H_2O_2) from the O_2 molecule. The associative and dissociative paths are the $4e^-$ transfer reaction pathways through which the ORR mechanism takes place. Overall the ORR is given by $O_2 + 4H^+ + 4e^- \rightarrow 2H_2O$.

$$\begin{aligned} O_2 &\rightarrow [L] - O_2 \\ &\rightarrow [L] - OOH \\ &\rightarrow [L] - O + H_2O\ (\text{or}\ H_2O_2) \\ &\rightarrow [L] - OH + H_2O \\ &\rightarrow 2H_2O \end{aligned} \tag{1}$$

$$\begin{aligned} O_2 &\rightarrow [L] - O_2 \\ &\rightarrow [L] - 2O \\ &\rightarrow [L] - O + [L] - OH \\ &\rightarrow [L] - O + H_2O\ (\text{or}\ H_2O_2) \\ &\rightarrow [L]{-}OH + H_2O \\ &\rightarrow 2H_2O \end{aligned} \tag{2}$$

In the above equations, L represents the catalyst's active adsorption site which adsorbs the O_2 molecule during the initial stage of the ORR. Eqs 1 and 2 illustrate the associative and dissociative reaction mechanisms of the ORR, respectively. Here, in the above equations, we neglected the addition of protons and electrons for simplicity. H_2O and H_2O_2 are the respective products of the $4e^-$ and $2e^-$ transfer reaction mechanisms of the ORR.

Theoretical Calculations and Equations. In our current investigation, the reaction steps of the O_2 reduction reaction have been explored on the surface of 2D monolayer $LaNiO_3$ with respect to the standard hydrogen electrode (SHE) or computational hydrogen electrode (CHE) model, which has been mentioned earlier. Therefore, the thermodynamical equations can be written as below to compute the relative free energy during the ORR.

$$G = E_{DFT} + E_{ZPE} + \int C_P\, dT - TS \tag{3}$$

The above (eq 3) was used to calculate the free energy of various intermediate species (G), where E_{DFT}, E_{ZPE}, and S are the ground-state electronic energy, zero-point vibrational energy, and entropy, respectively. T denotes the temperature which is 298.15 K in the present investigation.

$$\Delta G_{ads} = \Delta E_{ads} + \Delta E_{ZPE} - T\Delta S \tag{4}$$

The above eq 4 was used to calculate the change in the free energy of reaction intermediates (adsorbates) at pH = 0 where

https://doi.org/10.1021/acsomega.4c03544
ACS Omega 2024, 9, 35614−35626

ΔG_{ads} represents the adsorption free energy of adsorbates. ΔE_{ads}, ΔE_{ZPE}, and ΔS are the differences of electronic energy (E_{DFT}), zero-point vibrational energy (E_{ZPE}), and entropy (S), respectively. The contribution of specific heat capacity at constant pressure (C_P) was carried out in the free energy (G) calculation as expressed in eq 3. The value of the lattice specific heat capacity C_P was maintained constant at a temperature (T) equal to 298.15 K. The temperature (T) was taken to be constant while calculating the change of free energy during the H-adsorption. Thus, during the calculation of the change of free energy of the ORR steps, the integral part of $\int C_P \, dT$ was zero. The following eq 5 was used to calculate the free energy of O_2 as the DFT method could not describe the high-spin ground state of the oxygen molecule satisfactorily.

$$G_{O_2} = 2G_{H_2O} - 2G_{H_2} - 4.92 \quad (5)$$

RESULTS AND DISCUSSION

The equilibrium structure of the 3D bulk crystal of $LaNiO_3$ was obtained by the PBE-D3 method as shown in Figure 2a.

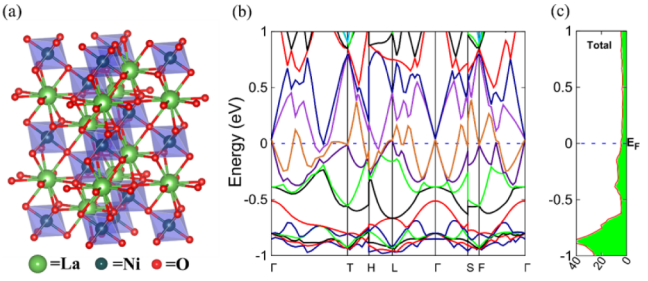

Figure 2. (a) Equilibrium crystal structure, (b) electronic band structure, and (c) total DOS of the 3D $LaNiO_3$ perovskite.

The optimized lattice constants and equilibrium bond angles of 3D $LaNiO_3$ were found to be $a = b = 5.48$ Å, $c = 13.04$ Å, $\alpha = \beta = 90°$, and $\gamma = 120°$. The bulk crystal structure of $LaNiO_3$ has a rhombohedral $R\bar{3}c$ space group symmetry. The equilibrium La−O and Ni−O bond lengths were 2.76 Å and 1.94 Å, respectively, obtained by the same method. The obtained lattice parameters are well consistent with the previous reported values.[50] The electronic property calculations, i.e., the electronic band structure and total density of states (DOS) of the bulk 3D $LaNiO_3$, were obtained by the same PBE-D3 method. A highly symmetric **Γ−*T*−*H*−*L*−Γ−*S*−*F*−Γ** direction was used to plot the electronic band structure and total DOS of 3D $LaNiO_3$ in the first Brillouin zone represented in Figure 2b,c. The electronic band structure and total DOS were calculated with respect to the Fermi energy level (E_F) while using the atomic orbital of La, Ni, and O atoms in DOS calculations.

We found that the 3D crystal structure of the $LaNiO_3$ perovskite has a zero electronic band gap from the property calculations, and the total DOS shows the presence of a high electron density around the Fermi level (E_F). Therefore, from both the band and DOS calculations, we can say that the 3D crystal structure of the $LaNiO_3$ perovskite is a good conductive material in nature. However, it could not be directly used as an electrocatalyst for the ORR because of the smaller exposed surface area. To address this, we computationally created a 2D monolayer $LaNiO_3$ from 3D $LaNiO_3$ by cleaving the (0 0 1) surface with a perpendicular 15 Å vacuum region along the z-direction to avoid symmetry in that direction. The height of the unit cell was maintained at 15 Å to fit the vacuum space to avoid periodicity. We cleaved the (0 0 1) surface from 3D $LaNiO_3$ because, according to previous studies, it enhances the catalytic activity of perovskite materials by decreasing the overpotential.[15]

Then, we utilized the PBE-D3 method to obtain the equilibrium geometry and electronic properties of the 2D monolayer $LaNiO_3$. Figure 3a represents the equilibrium

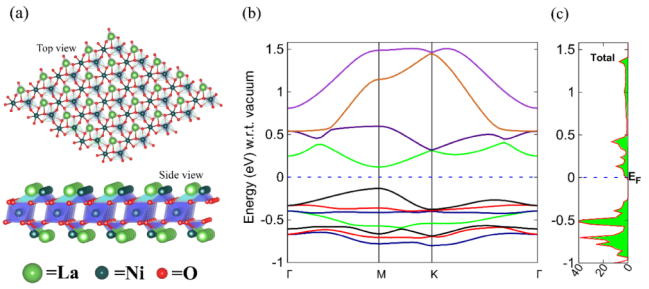

Figure 3. (a) Top and side view, (b) electronic band structure, and (c) total DOS of the equilibrium 2D monolayer $LaNiO_3$.

structure of the 2D monolayer $LaNiO_3$. In this study, we have utilized a 1 × 1 unit cell of the 2D monolayer $LaNiO_3$ system defined by the lattice parameters $a = b = 5.58$ Å, $\alpha = \beta = 90°$, and $\gamma = 120°$, respectively. We observed that the equilibrium structure of the 2D monolayer $LaNiO_3$ perovskite has a trigonal $P\bar{3}$ layer group symmetry. Additionally, the optimized La−O bond length was 2.56 Å, and the Ni−O bond distance was 1.94 Å. The electronic band structure and total DOS of 2D monolayer $LaNiO_3$ were calculated w.r.t. vacuum using a highly symmetric **Γ−*M*−*K*−Γ** path. In our study, we have selected a highly symmetric k-vector path to compute the electronic properties, i.e., the electronic band structure and total DOS of the 2D monolayer $LaNiO_3$ and various reaction intermediates of the ORR. The k-paths are the high-symmetry paths in the reciprocal space that are frequently used to compute the electronic band structures in the periodic solids, and they are essential for studying the physical characteristics. Due to processing limitations, energy bands are usually calculated along high-symmetry line segments in the irreducible Brillouin zone followed by the original symmetry of the system. The stationary points in a band structure can be found along the high-symmetry points and line segments within the Brillouin zone to avoid the crossings in the energy spectrum. In the present work, the highly symmetric k-path is well consistent with the symmetry of our studied material. The selection of a high symmetric k-vector path reduces the computational time and resources compared to computing energies across the entire boundary, making it feasible to explore the dispersion landscape efficiently. The energy band structure and total density of states of the 2D monolayer $LaNiO_3$ are illustrated in 3b,c. Table 1 summarizes the equilibrium lattice constants, band gap, bond lengths, and space group symmetry of 2D monolayer $LaNiO_3$ and 3D $LaNiO_3$ with the earlier reported results. From our DFT calculations of the 2D monolayer $LaNiO_3$, we found that it has an indirect band gap of 0.25 eV, and there is a low electron density of states around the Fermi energy level in the total density of states, confirming that it is a very low band gap semiconducting material.

https://doi.org/10.1021/acsomega.4c03544
ACS Omega 2024, 9, 35614−35626

Table 1. Equilibrium Lattice Parameters of 3D $LaNiO_3$ and 2D Monolayer $LaNiO_3$

System	Lattice constant (Å)	Angles (in degree)	Space group	Bond distance (Å)	Band gap (E_g)	Ref
3D bulk $LaNiO_3$	$a = b = 5.48$	$\alpha = \beta = 90$,	$R\bar{3}c$	La−O = 2.76	0.00	this work
	$c = 13.04$	$\gamma = 120$		Ni−O = 1.94		
2D monolayer $LaNiO_3$	$a = 5.58$	$\alpha = 89.93$,	$P\bar{3}$	La−O = 2.56	0.25	this work
	$b = 5.58$	$\beta = 90.05$,		Ni−O = 1.94		
		$\gamma = 120.07$				
3D $LaNiO_3$(previous work)	$a = b = 5.45$	$\alpha = \beta = 90$,	$R\bar{3}c$	Ni−O = 1.93	0.00	15
	$c = 13.14$	$\gamma = 120$				

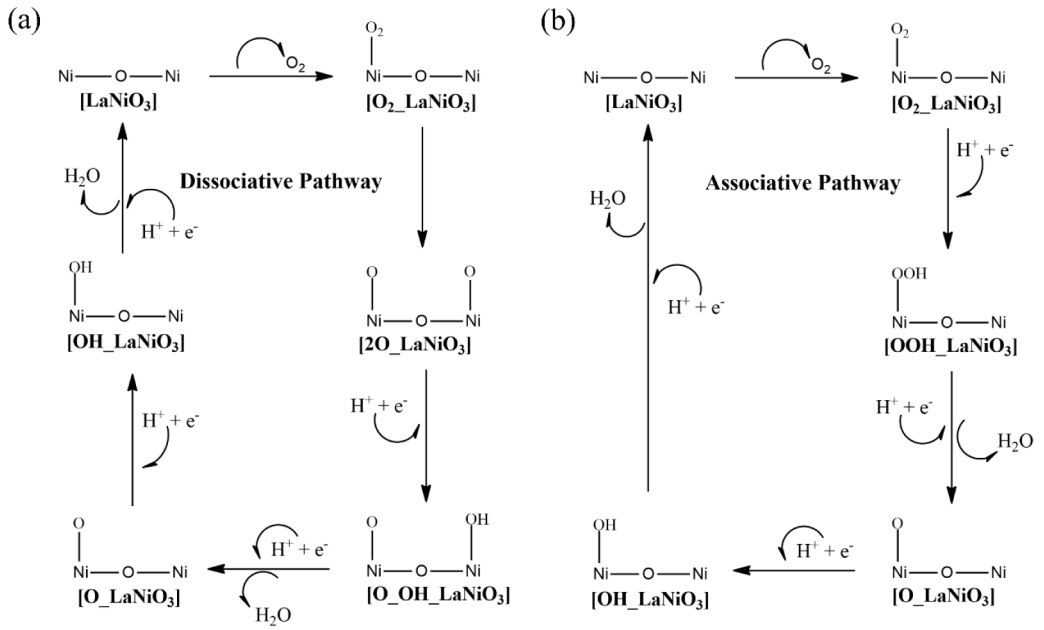

Figure 4. Schematic representation of (a) dissociative and (b) associative reaction pathways of the ORR on the surface of the 2D monolayer $LaNiO_3$ with the $4e^-$ transfer mechanism.

ORR Mechanisms. From the electronic property calculations of the 2D monolayer $LaNiO_3$, we confirmed that it is a very low band gap semiconductor in nature, and it may have good catalytic activity because of less band gap and the presence of electron density around the Fermi energy level. Therefore, the electrons can easily transfer from the valence bands to the conduction bands, and the charge transfer is easy during the chemical reactions (especially electrochemical reactions) on its surface. To know whether this 2D monolayer $LaNiO_3$ perovskite is a suitable candidate for catalyzing the ORR, we started exploring the ORR mechanisms on the surface of the 2D monolayer $LaNiO_3$ by creating various reaction intermediates computationally. Figure 4a,b represents the schematic diagram of the proposed four-electron ($4e^-$) transfer mechanisms of the ORR performed on the surfaces of 2D monolayer $LaNiO_3$ that can follow either dissociative or associative pathways. Here, in Figure 4, both the dissociative and associative pathways are shown with all of the reaction intermediates involved during the O_2 reduction reaction. The consecutive reaction steps with the addition of electrons (e^-), protons (H^+), and removal of water (H_2O) molecules are represented by various arrows.

During the adsorption of the O_2 molecule on the Ni site of the 2D monolayer $LaNiO_3$, charge transfer occurs between the oxygen (O) and the nickel (Ni) atoms. The charge transfer from the Ni atom to the O atom is necessary for the initiation of the O_2 reduction reaction. The electronic charge variation on the Ni and O centers during the reaction was verified through charge difference density and Bader charge analysis.[51] We found that the charge on the Ni atom before the O_2 adsorption was 0.692e. After the O_2 adsorption, the charge on the Ni atom was 1.043e; where e is the charge of an electron. Similarly, the charge on the oxygen atom (which is bonded to the Ni atom) before and after the O_2 adsorption was −0.011e and −0.470e, respectively. So, 0.351e unit of charge was transferred from the Ni atom to the O atom during the O_2 adsorption step. Figure 5 shows the charge difference density of the O_2_$LaNiO_3$ reaction intermediate, where the yellow and cyan regions represent charge depletion and accumulation, respectively.

Dissociative Reaction Pathway. The most important issue during the ORR process is the number of exposed active sites for the adsorption of the O_2 adsorbate, which determines the ORR activity. All of the reaction intermediates that occur during the ORR mechanisms followed by the dissociative pathway on the surface of the 2D monolayer $LaNiO_3$ are shown in Figure 6. A solvent can influence a chemical reaction in various ways, such as by changing the reaction rate, modifying the geometry of the reactants, altering the energy landscape of the reaction, and affecting the stability of the intermediates. This issue can be resolved by using gas phase modeling, which involves modeling individual molecules or small clusters of molecule's behavior in a gaseous environment under controlled conditions. Under these conditions, DFT

https://doi.org/10.1021/acsomega.4c03544
ACS Omega 2024, 9, 35614−35626

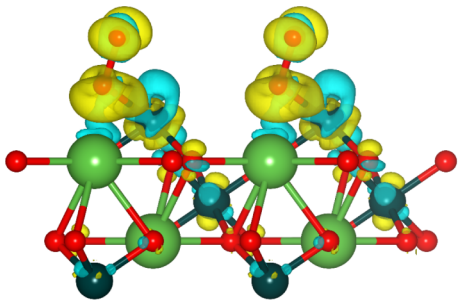

Figure 5. Charge difference density of O_2 adsorbed on the Ni atom of the 2D monolayer $LaNiO_3$ perovskite, i.e., the O_2_$LaNiO_3$ reaction intermediate. The yellow region denotes charge depletion, and the cyan color denotes charge accumulation.

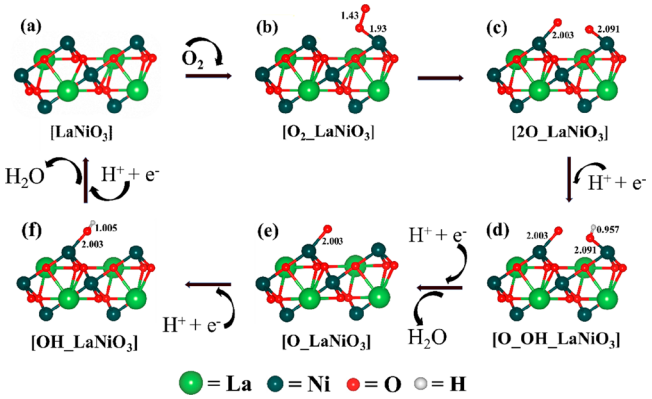

Figure 6. Equilibrium structures of all of the reaction intermediates involved in the dissociative pathway of the ORR on the surface of the 2D monolayer $LaNiO_3$ perovskite.

computations are easier and more accurate even in a gas−solid interface. We initialized the modeling of the O_2 reduction reaction steps on the active exposed surface of the 2D monolayer $LaNiO_3$ computationally for further calculations under computational hydrogen electrode conditions (CHE) i.e., H_2 pressure is 1 bar with zero pH.

The initial step of the ORR involves the adsorption of the O_2 molecule on the surface of 2D monolayer $LaNiO_3$ at the nickel site, which leads to the formation of a reaction intermediate represented by O_2_$LaNiO_3$ with the change in free energy (ΔG) equal to −0.66 eV as shown in Figure 6b. The free energy calculation indicates that the adsorption of O_2 on the surface of 2D monolayer $LaNiO_3$ at the nickel site is thermodynamically feasible as the relative free energy (ΔG) is negative (Figure 7). The calculated equilibrium bond lengths La−O and Ni−O of the O_2_$LaNiO_3$ reaction intermediate were found to be 2.61 Å and 1.93 Å, respectively. The optimized O−O bond length was 1.43 Å. In the next step, the extended bond between oxygen atoms in the adsorbed O_2 of reaction intermediate O_2_$LaNiO_3$ is broken, leading to the adsorption of one oxygen atom onto a distinct Ni site, resulting in the formation of new reaction intermediate 2O_$LaNiO_3$. In the 2O_$LaNiO_3$ reaction intermediate, the two activated oxygen atoms attach to two distinct Ni sites of the 2D monolayer $LaNiO_3$ perovskite. The equilibrium lattice parameters of all the reaction intermediates of the ORR involved during the dissociative mechanism are reported in Table 2.

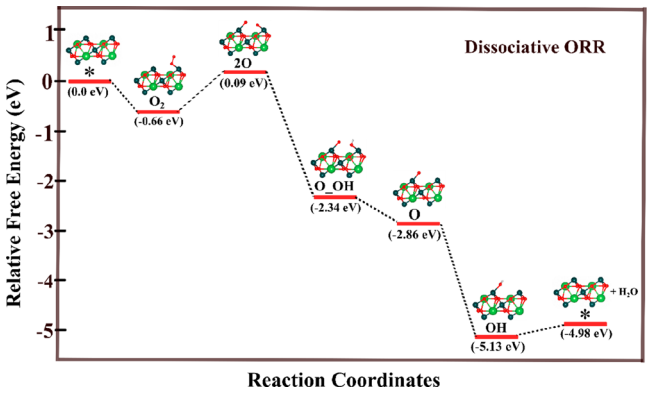

Figure 7. Relative free energy profiles for the dissociative mechanism of the ORR on the surface of the 2D monolayer $LaNiO_3$ perovskite.

In this study, the transition state (TS) during the O_2 dissociation step was obtained by using the climbing-image nudged elastic band (CI-NEB) method.[52,53] The approximate path of O_2 dissociation was generated, and one intermediate image was relaxed. We found that the cleavage of the O−O bond occurs with a transition state (TS) during the O_2 dissociation step. Figure 8 represents the free energy profile for the dissociation of O_2 on the surface of 2D monolayer $LaNiO_3$ with the transition state (TS). We found that the O_2 dissociation barrier was +1.42 eV during the cleavage of the O−O bond. There is a complex interaction between the O_2 molecule and the Ni atoms on the surface of the 2D monolayer $LaNiO_3$ perovskite during the ORR mechanism. In the $LaNiO_3$ perovskite, Ni has a +3 oxidation state. The O−O cleavage process occurs after the adsorption of the O_2 molecule on the Ni atom of the 2D monolayer $LaNiO_3$. The O_2 molecule dissociates into two activated oxygen atoms, and they get attached to two different Ni atoms on the surface of the 2D monolayer $LaNiO_3$. The oxygen atom having a −2 oxidation state forms a bond with the Ni atom. This involves charge transfer from the oxygen atom to the Ni atom, due to which Ni reduces from the +3 to +2 oxidation state. Hence, to accommodate the additional negative charge from the oxygen atom during the O−O cleavage process, the oxidation state of Ni changes from Ni^{3+} to Ni^{2+}.

The equilibrium structure of the 2O_$LaNiO_3$ reaction intermediate is depicted in Figure 6c and the relative free energy profile for the dissociative mechanism of the ORR is represented in Figure 7. The completion of this reaction step ($O_2 \rightarrow 2O$) has occurred with a change of relative free energy (ΔG) of 0.09 eV which indicates that this step is endothermic in nature. We found that in equilibrium 2O_$LaNiO_3$ intermediate, the La−O and Ni−O bond distances are 2.56 Å and 2.01 Å, respectively. The reaction intermediate 2O_$LaNiO_3$ is unstable, as the relative free energy required for its formation is positive. In the next step, one adsorbed oxygen atom at the nickel site gets reduced to form a hydride ion (OH^-) on the perovskite surface, giving the O_OH_$LaNiO_3$ reaction intermediate as depicted in Figure 6d. Our study demonstrates that the O−H bond length is 0.95 Å, and both the equilibrium La−O and Ni−O bond lengths remain unchanged i.e., 2.56 Å and 2.01 Å, respectively. The relative free energy change in this reaction step is about −2.34 eV as depicted in Table 3.

The formation of the O_OH_$LaNiO_3$ intermediate from 2O_$LaNiO_3$ involves the transfer of an electron from the

https://doi.org/10.1021/acsomega.4c03544
ACS Omega 2024, 9, 35614−35626

Table 2. Equilibrium Lattice Parameters and Space Group Symmetry of All the Reaction Intermediates of the Dissociative Mechanism in the ORR Process

System	Lattice constants (Å)	Angles (in degree)	Space group symmetry	The band gap (eV)	Average bond distances (Å) La−O	Ni-O	O−O	O-H
O_2_$LaNiO_3$	a = 5.58	α = 79.46	*P1*	0.10	2.61	1.93	1.43	-
	b = 5.15	β = 97.06						
		γ = 116.36						
2O_$LaNiO_3$	a = 5.48	α = 87.12	*P1*	0.00	2.56	2.01	-	-
	b = 5.40	β = 96.74						
		γ = 126.45						
O_OH_$LaNiO_3$	a = 5.52	α = 84.27	*P1*	0.01	2.56	2.01	-	0.95
	b = 5.46	β = 94.74						
		γ = 120.22						
O_$LaNiO_3$	a = 5.54	α = 89.92	*P1*	0.13	2.56	1.97	-	-
	b = 5.43	β = 89.96						
		γ = 119.82						
OH_$LaNiO_3$	a = 5.62	α = 91.14	*P1*	0.76	2.56	1.97	-	1.00
	b = 5.48	β = 92.41						
		γ = 121.26						
OOH_$LaNiO_3$	a = 5.62	α = 95.76	*P1*	0.00	2.52	1.88	1.30	0.96
	b = 5.90	β = 80.47						
		γ = 125.26						

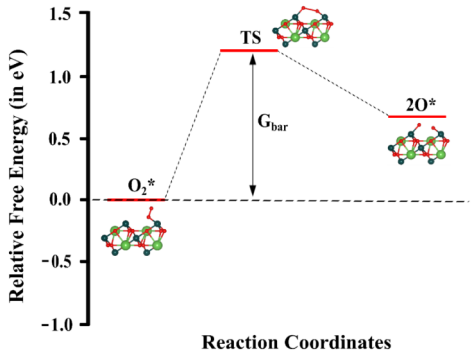

Figure 8. O_2 dissociation on the surface of 2D monolayer $LaNiO_3$ with a transition state (TS).

Table 3. All the Reaction Intermediates of Dissociative Pathways of the ORR Along with the Change in their Free Energy (ΔG) Occurring on the Surface of the 2D Monolayer $LaNiO_3$ Perovskite

O_2 reduction reaction steps	ΔG (in eV)	Reaction intermediates	Relative free energies (in eV)
[$LaNiO_3$] → [O_2_$LaNiO_3$]	−0.66	O_2_$LaNiO_3$	−0.66
[O_2_$LaNiO_3$] → [2O_$LaNiO_3$]	0.76	2O_$LaNiO_3$	0.09
[2O_$LaNiO_3$] → [O_OH_$LaNiO_3$]	−2.44	O_OH_$LaNiO_3$	−2.34
[O_OH_$LaNiO_3$] → [O_$LaNiO_3$]	−0.51	O_$LaNiO_3$ + H_2O	−2.86
[O_$LaNiO_3$] → [OH_$LaNiO_3$]	−2.27	OH_$LaNiO_3$	−5.13
[OH_$LaNiO_3$] → [$LaNiO_3$]	0.15	$LaNiO_3$ + H_2O	−4.98

electrode to one adsorbed oxygen atom on the surface of the perovskite, which reduces it to a hydride ion via the addition of one proton. Now, the hydride ion reacts with a proton (H^+) and electron (e^-) to form a water (H_2O) molecule with a free energy change of −0.51 eV and the relative free energy change of about −2.86 eV, giving the reaction intermediate O_$LaNiO_3$ as shown in Figure 4a. Here, the equilibrium La−O bond length is 2.56 Å, and the Ni−O bond length decreases to 1.97 Å. The equilibrium structure of reaction intermediate O_$LaNiO_3$ is shown in Figure 6e. The addition of one electron and proton to the O_$LaNiO_3$ reaction intermediate results in the formation of the OH_$LaNiO_3$ intermediate with an energy cost of −2.27 eV. In the last step of the dissociative mechanism, the addition of one more electron and proton with reaction intermediate OH_$LaNiO_3$ results in the removal of the second water molecule as depicted in Figure 4a with the change of free energy of about 0.15 eV. Equilibrium lattice parameters of all the reaction intermediates of the ORR involved in the dissociative mechanism are listed in Table 2. The change in the free energy of each reaction step and the relative free energy of different reaction intermediates are listed in Table 3.

A Review of the Different Stages of the ORR Mechanism. Step 1: The VASP suit code with the PBE-D3 method was used to obtain the equilibrium geometry of the O_2_$LaNiO_3$ reaction intermediate, which is represented in Figure 6b. The oxygen molecule is adsorbed on the surface of the 2D monolayer $LaNiO_3$ perovskite at the Ni site because nickel has a higher density of electrons which is favorable for O_2 adsorption. Computationally, the reaction intermediate O_2_$LaNiO_3$ was examined, and we found that the La−O, Ni−O, and O−O bond distances were 2.61 Å, 1.93 Å, and 1.43 Å, respectively. We found that the equilibrium structure of the O_2_$LaNiO_3$ reaction intermediate has a *P1* layer group symmetry with lattice parameters a = 5.58 Å, b = 5.15 Å, α = 79.46°, β = 97.06°, and γ = 116.36°, respectively, as given in Table 2. The electronic band structure and total DOS of the O_2_$LaNiO_3$ reaction intermediate is illustrated in Figure 9a, which is plotted using a high-symmetry Γ−M−K−Γ direction. The energy band structure and total density of states are normalized, i.e., computed with respect to the Fermi level (E_F). The eigenvalues of the valence band maximum (VBM) and conduction band maximum (CBM) were −0.95 eV and −0.85 eV. The calculated energy band gap was found to be 0.10 eV (indirect band gap), and in the total DOS, there is a small

https://doi.org/10.1021/acsomega.4c03544
ACS Omega 2024, 9, 35614−35626

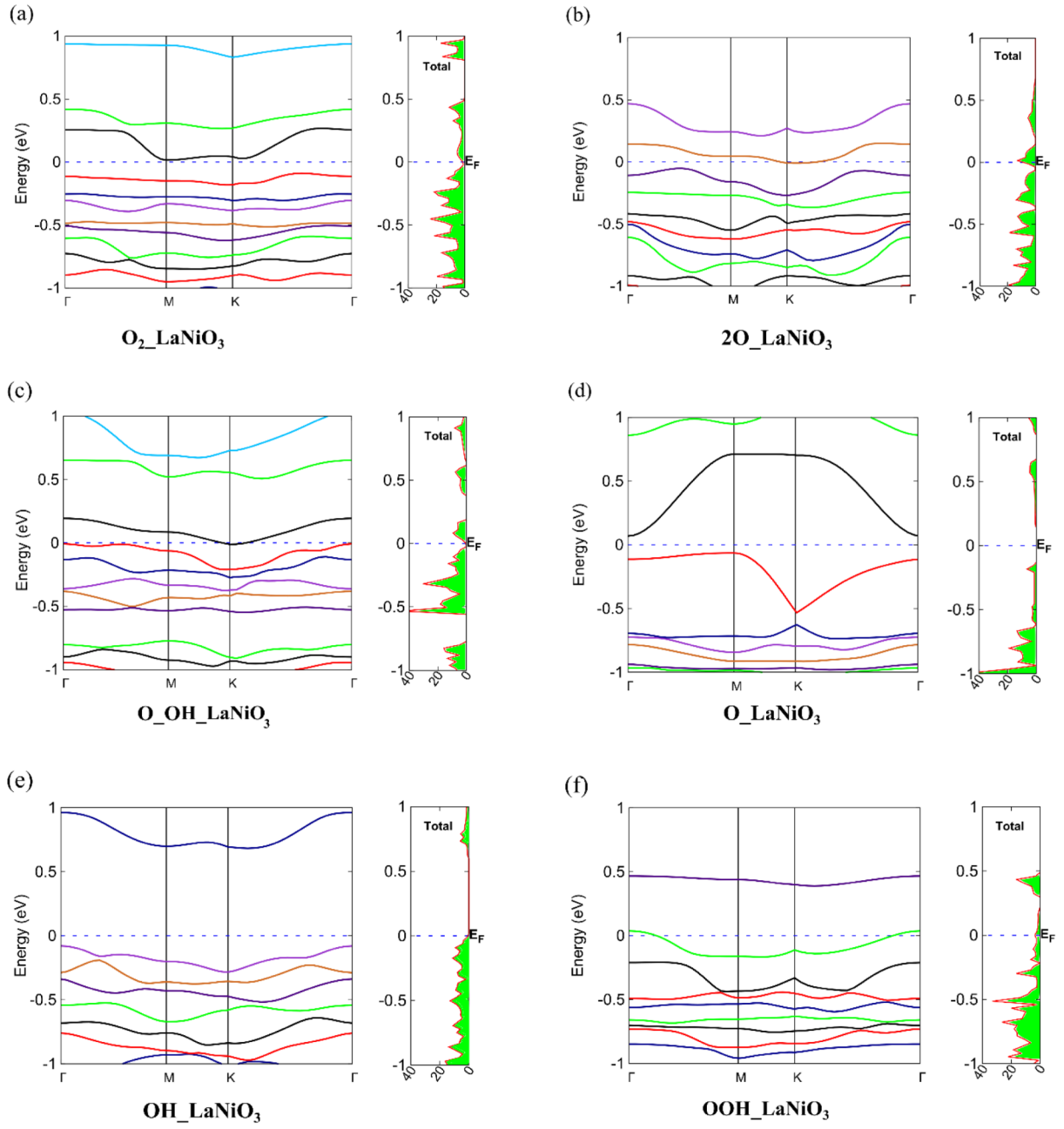

Figure 9. Electronic band structure and total DOS of (a) O_2_LaNiO_3, (b) 2O_LaNiO_3, (c) O_OH_LaNiO_3, (d) O_LaNiO_3, and (e) OH_LaNiO_3 reaction intermediates of the dissociative pathway, and (f) OOH_LaNiO_3 reaction intermediate of the associative ORR mechanism on the surface of the 2D monolayer LaNiO_3 perovskite.

electron density present near the Fermi level showing the conducting properties of the O_2_LaNiO_3 reaction intermediate.

Step 2: In this step, the equilibrium structure of the 2O_LaNiO_3 reaction intermediate was achieved through the dissociation of the O−O bond in the O_2_LaNiO_3 reaction intermediate. This process was followed by the migration of a single oxygen atom to an adjacent Ni site within the 2D LaNiO_3 perovskite structure. The equilibrium structure of the 2O_LaNiO_3 reaction intermediate is shown in Figure 6c. The equilibrium lattice parameters of 2O_LaNiO_3 are a = 5.48 Å, b = 5.40 Å, α = 87.12°, β = 96.74°, and γ = 126.45°, and it has a *P1* layer group symmetry. Here, the equilibrium La−O bond distance is decreased by 0.05 Å and the Ni−O bond distance is elongated by 0.08 Å, respectively. The electronic band structure and total DOS of 2O_LaNiO_3 were plotted w.r.t. vacuum using the high-symmetry **Γ−*M*−*K*−Γ** path. The eigenvalues of the VBM and CBM were −0.65 eV. The calculated energy band gap is zero, meaning that this intermediate completely behaves like a conductor. The total DOS of the 2O_LaNiO_3 reaction intermediate has electron density of states around the Fermi level (E_F), as depicted in Figure 9b.

Step 3: The equilibrium structure of the O_OH_LaNiO_3 reaction intermediate is shown in Figure 6d. The formation of O_OH_LaNiO_3 takes place when an electron and proton react with the 2O_LaNiO_3 intermediate. The present calculation reveals that equilibrium O_OH_LaNiO_3 has *P1* symmetry.

https://doi.org/10.1021/acsomega.4c03544
ACS Omega 2024, 9, 35614−35626

The equilibrium La−O, Ni−O, and O−H bond lengths are 2.56 Å, 2.01 Å, and 0.95 Å, respectively. Here, the lattice parameters, i.e., lattice constants and bond angles, were found to be a = 5.52 Å, b = 5.46 Å, α = 84.27°, β = 94.74°, and γ = 120.22°, respectively. A highly symmetric k-vector **Γ−*M*−*K*−Γ** path was used to compute the electronic band structure and total DOS of the O_OH_$LaNiO_3$ reaction intermediate by using the PBE-D3 method. Here, the eigenvalues obtained for the VBM and CBM were −0.95 eV and −0.94 eV. The band gap was found to be about 0.01 eV. Figure 9c represents the electronic band structure and total DOS of the O_OH_$LaNiO_3$ reaction intermediate.

Step 4: In the next step, the addition of one proton and one electron to the O_OH_$LaNiO_3$ reaction intermediate results in the removal of one water molecule from the surface of 2D $LaNiO_3$ with the formation of the O_$LaNiO_3$ reaction intermediate. Figure 6e shows the equilibrium structure of the O_$LaNiO_3$ reaction intermediate which has *P1* symmetry. The equilibrium lattice parameters of the O_$LaNiO_3$ intermediate were a = 5.54 Å, b = 5.43 Å, α = 89.92°, β = 89.96°, and γ = 119.82°, respectively. The equilibrium Ni−O and La−O bond distances were found to be 1.97 and 2.56 Å. The electronic properties, i.e., the band structure and total DOS of the O_$LaNiO_3$ reaction intermediate were calculated w.r.t vacuum using a high-symmetry **Γ−*M*−*K*−Γ** direction. In Figure 9d, the electronic band structure and total DOS of the O_$LaNiO_3$ reaction intermediate are normalized. The eigenvalues of the VBM and CBM were −0.97 eV and −0.84 eV. Our study found that the O_$LaNiO_3$ reaction intermediate has a band gap of about 0.13 eV. A small band gap of this reaction intermediate shows good conductivity for mass electron and charge transfer during the chemical reaction.

Step 5: The formation of the last reaction intermediate OH_$LaNiO_3$ in the dissociative mechanism of the ORR results via the addition of one proton and electron to the O_$LaNiO_3$ intermediate, where the activated oxygen atom attached to the Ni site forms a bond with the hydrogen atom. The equilibrium structure of the OH_$LaNiO_3$ reaction intermediate is shown in Figure 6f, and it acquired *P1* layer group symmetry. The equilibrium lattice parameters were found to be a = 5.62 Å, b = 5.48 Å, α = 91.14°, β = 92.41°, and γ = 121.26°, respectively. The equilibrium bond distance between the hydrogen and the oxygen atoms was 1.0 Å. The normalized electronic band structure and total DOS of the OH_$LaNiO_3$ reaction intermediate are represented in Figure 9e, which has a band gap of about 0.76 eV. In this case, the eigenvalues of the VBM and CBM were −0.53 eV and 0.23 eV. We can see a small electron density around the Fermi level (E_F). Furthermore, the addition of one more electron and proton to the OH_$LaNiO_3$ reaction intermediate results in the formation of the second water (H_2O) molecule, and 2D monolayer $LaNiO_3$ is ready for further O_2 adsorption at the nickel site, and the reaction steps continue. Hence, a total of four electrons and four protons are used to reduce the O_2 molecule into two water molecules in the ORR mechanism.

Associative Reaction Pathway. Additionally, we studied the associative O_2 reduction reaction mechanism computationally on the surface of the 2D monolayer $LaNiO_3$ perovskite. The initial step of the ORR involves the adsorption of the O_2 molecule at the Ni site, giving the O_2_$LaNiO_3$ reaction intermediate. The initial O_2 adsorption step in the associative path is similar to the first step of the dissociative mechanism. A schematic representation of the ORR associative mechanism is illustrated in Figure 4b. In contrast to the dissociative mechanism where O_2 dissociates into 2O (two activated oxygen atoms), here in the associative mechanism, one hydrogen gets attached to the O_2 molecule giving the OOH_$LaNiO_3$ reaction intermediate due to the reaction of the adsorbed oxygen molecule with one electron and one proton. The equilibrium structure of the OOH_$LaNiO_3$ reaction intermediate is shown in Figure 10c.

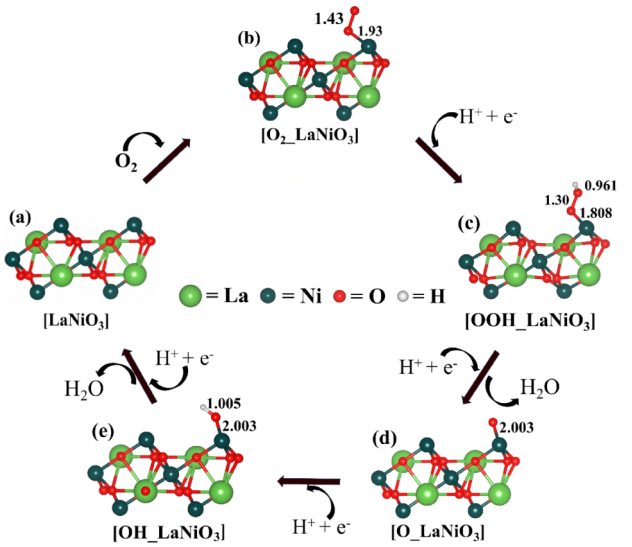

Figure 10. Equilibrium structures of all the reaction intermediates involved in the associative reaction pathway of the ORR taken place on the surface of the 2D monolayer $LaNiO_3$ perovskite.

The formation of the OOH_$LaNiO_3$ reaction intermediate from the O_2_$LaNiO_3$ intermediate takes place with a free energy change of −1.99 eV, whose value is negative, which implies that this step does not require any additional energy input. It means the occurrence of this reaction step is spontaneous and thermodynamically favorable. Figure 10 illustrates all of the equilibrium structures of reaction intermediates involved in the associative mechanism of the ORR on the surface of the 2D monolayer $LaNiO_3$. Computationally, after the structure relaxation of the OOH_$LaNiO_3$ reaction intermediate, we found that it has *P1* symmetry. The lattice parameters, i.e., lattice constant and bond angles, were a = 5.62 Å, b = 5.90 Å, α = 95.76°, β = 80.47°, and γ = 125.26°, respectively. The equilibrium La−O, Ni−O, and O−O bond lengths were 2.52 Å, 1.88 Å, and 1.30 Å, respectively. The equilibrium bond distance between the oxygen and hydrogen atoms was 0.96 Å. The electronic band structure and total DOS of the OOH_$LaNiO_3$ reaction intermediate are shown in Figure 9f, which are computed using a high symmetric **Γ−*M*−*K*−Γ** direction. We found that the equilibrium structure of the OOH_$LaNiO_3$ reaction intermediate has a zero band gap and there is a small electron density of states present near the Fermi level (E_F). In the further step, the addition of one electron (e^-) and one proton (H^+) to the OOH_$LaNiO_3$ reaction intermediate gives the O_$LaNiO_3$ reaction intermediate with the removal of one water (H_2O) molecule with a free energy change of −0.21 eV as represented in Figure 4b. The equilibrium structure of the O_$LaNiO_3$ reaction intermediate is depicted in Figure 10d. The negative value of the Gibb's free energy change clarifies that the occurrence of this reaction step is spontaneous, i.e., does not

https://doi.org/10.1021/acsomega.4c03544
ACS Omega 2024, 9, 35614−35626

require any additional energy inputs, and is thermodynamically favorable.

In a further step, the OH_$LaNiO_3$ reaction intermediate is formed by the protonation of the O_$LaNiO_3$ intermediate, where the activated oxygen atom reacts with one electron and proton. The amount of energy required for this step to occur is −2.28 eV. The equilibrium structure of the OH_$LaNiO_3$ reaction intermediate is shown in Figure 10e. In the last step of the associative O_2 reduction reaction, one more electron and proton reacts with the OH_$LaNiO_3$ intermediate which results in the removal of the second water (H_2O) molecule at a free energy cost of 0.15 eV as depicted in Figure 4b. The relative free energy profile for the reaction intermediates of the associative mechanism of the ORR is shown in Figure 11.

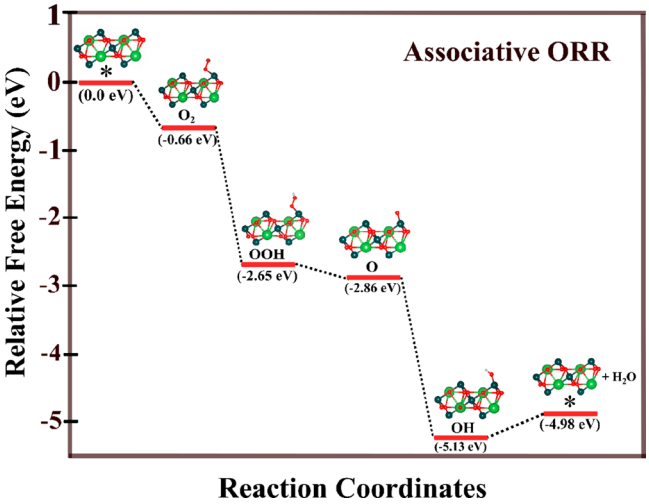

Figure 11. Relative free energy profiles for the associative mechanism of the ORR on the surface of 2D monolayer $LaNiO_3$.

Here, four electrons and four protons are utilized to complete the whole ORR mechanism by reducing the O_2 molecule on the surface of the 2D monolayer $LaNiO_3$ perovskite, producing two water molecules. The relative free energy and Gibb's free energy (ΔG) of various reaction intermediate steps during the associative pathway of the ORR are listed in Table 4.

In this study, we investigated the ORR mechanism on the surface of the 2D monolayer $LaNiO_3$ perovskite. The ORR occurs through a four-electron ($4e^-$) reduction mechanism on the surface of the 2D monolayer $LaNiO_3$ followed by two mechanisms: (a) associative and (b) dissociative. To get a better understanding of thermodynamics related to a chemical reaction, we have computed and examined the relative Gibbs free energy (ΔG) of each reaction step of the ORR. The dissociative pathway, which involves the dissociation of the O_2 molecule into two activated oxygen atoms after the O_2 adsorption, has been studied followed by the $4e^-$ transfer mechanism. We found that the change of Gibbs free energy (ΔG) during the reaction step involving O_2 dissociation ($O_2 \rightarrow 2O$) after O_2 adsorption was 0.76 eV. The positive value of ΔG signifies that the O_2 dissociation reaction step is endothermic which means an additional energy input is required for this step to proceed the ORR, whereas the associative pathway involves the formation of an OOH reaction intermediate after the O_2 adsorption. We found that reaction intermediate OOH_$LaNiO_3$ formed from the O_2_$LaNiO_3$ intermediate with a value of ΔG of about −1.99 eV, which is negative. The negative value of ΔG signifies that this reaction step is exothermic which means this step is spontaneous and no external energy input is needed in this ORR step. Comparing the values of ΔG in both the cases, we can conclude that the most thermodynamic favorable pathway will be the one whose reaction step is spontaneous and energetically favorable. Hence, the associative reaction pathway of the ORR on the surface of 2D monolayer $LaNiO_3$ is thermodynamically more favorable than the dissociative pathway.

If a particular step in the ORR process has a positive Gibbs free energy ($\Delta G > 0$), it indicates that the step is endergonic in nature under the standard conditions. Oxidation−reduction reactions, commonly known as redox reactions, are reactions that involve the transfer of electrons from one species to another. The species that loses electrons is said to be oxidized, while the species that gains electrons is said to be reduced. The driving force for a redox reaction is the difference in the electric potential of the two substances that are involved in electron transfer. In the subject reaction, the last step of the ORR in both dissociative and associative reaction pathways is [OH_$LaNiO_3$] → [$LaNiO_3$] + H_2O with an energy cost (ΔG) of about 0.15 eV obtained by the PBE-D3 method as reported in Tables 3 and 4. Therefore, the driving force of this step is simple, the difference in the electric potential of these two consecutive reaction steps which is $|\Delta G/e| = 0.15$ V. The positive value of ΔG of the last reaction step ([OH_$LaNiO_3$] → [$LaNiO_3$] + H_2O) of both the ORR pathways is favorable for the easy desorption of the H_2O molecule from the surface of the 2D monolayer $LaNiO_3$ perovskite; where the relative value of free energy of this step is about −4.98 eV as reported in Tables 3 and 4.

Table 4. All the Reaction Intermediates in the Associative Mechanism of the ORR Along with Their Gibb's Free Energy (ΔG) and Relative Free Energy

O_2 reduction reaction steps	ΔG (in eV)	Reaction intermediates	Relative free energies (in eV)
[$LaNiO_3$] → [O_2_$LaNiO_3$]	−0.66	O_2_$LaNiO_3$	−0.66
[O_2_$LaNiO_3$] → [OOH_$LaNiO_3$]	−1.99	OOH_$LaNiO_3$	−2.65
[OOH_$LaNiO_3$] → [O_$LaNiO_3$]	−0.21	O_$LaNiO_3$ + H_2O	−2.86
[O_$LaNiO_3$] → [OH_$LaNiO_3$]	−2.28	OH_$LaNiO_3$	−5.13
[OH_$LaNiO_3$] → [$LaNiO_3$]	0.15	$LaNiO_3$ + H_2O	-4.98

Theoretical Overpotential. Overpotential is the minimum additional potential required for the ORR to occur and effectively signifies the likelihood of an ORR taking place.[54−61] Overpotential can be calculated using the following eq 6,

$$\eta^{ORR} = 1.23 - \min(\Delta G \text{ of ORR steps})/e \quad (6)$$

Here, the rate-determining step is the OH desorption step which produces the second water molecule that again makes the catalyst's surface ready for further O_2 adsorption. The overpotential was found to be 1.08 V.

CONCLUSIONS

In our present study, we used DFT-D3 calculations to investigate the electronic structure and properties of the 3D bulk $LaNiO_3$ perovskite. From the electronic property

https://doi.org/10.1021/acsomega.4c03544
ACS Omega 2024, 9, 35614−35626

calculations of the 3D $LaNiO_3$ system, we found that it has conducting properties with a zero band gap and a large electron density is present around the Fermi level (E_F) in the total density of states. However, this property alone is not sufficient for it to be used as an electrocatalyst for the ORR as it has a less active surface area. To address this, we computationally designed a 2D monolayer $LaNiO_3$ from the 3D $LaNiO_3$ by cleaving the (0 0 1) surface to increase the active surface area. Additionally, we made a vacuum space perpendicular to the 2D single-layer $LaNiO_3$ slab to avoid spurious interactions between different layers, i.e., two consecutive layers. Using the PBE-D3 method, we studied the structural and electronic properties of 2D monolayer $LaNiO_3$ to determine its catalytic activity. Then, we computationally explored the mechanism of the ORR on the surface of the 2D monolayer $LaNiO_3$ by realizing different reaction intermediates at each step. Theoretically, we calculated Gibbs free energy and relative free energies of various reaction intermediates occurring in the ORR mechanisms. As per our study, the ORR mechanism follows both the associative and the dissociative reaction pathways on the surface of the 2D monolayer $LaNiO_3$ slab. In the dissociative pathway of the ORR, all of the reaction steps in the potential energy surface are downhill except during the O_2 dissociation step, whereas in the case of the associative pathway, we obtained negative free energies with downhill in the PES for each reaction step. All the ORR steps are spontaneous and thermodynamically favorable, which shows the suitable catalytic properties of the 2D monolayer $LaNiO_3$ for reducing O_2 molecules to water. Our energy calculations demonstrate that 2D monolayer $LaNiO_3$ has excellent catalytic properties for catalyzing oxygen reduction reaction through the $4e^-$ transfer mechanism. To sum up, our findings indicate that the 2D monolayer $LaNiO_3$ exhibits high electrocatalytic activity, making it a highly promising candidate for fuel cells and other energy conversion devices that require efficient ORR catalysts. The theoretical calculations performed in this study provide insight into the fundamental mechanisms and thermodynamics of the ORR on the surface of 2D monolayer $LaNiO_3$. It should be noted here that the active basal plane of 2D monolayer $LaNiO_3$ perovskite exhibits excellent catalytic activity toward the ORR with a high four-electron reduction pathway selectivity. These results suggest that it breaks the catalytic performance of the Pt-free electrodes with a high surface area and makes it a favorable contestant for fuel cell elements in renewable technology. We hope that our findings in this study are useful for developing new and more efficient non-noble metal-based electrocatalysts that can help meet the growing energy demand for clean and renewable energy sources.

■ ASSOCIATED CONTENT

Supporting Information

The Supporting Information is available free of charge at https://pubs.acs.org/doi/10.1021/acsomega.4c03544

All the equilibrium structures involved in the subject reaction (PDF)

■ AUTHOR INFORMATION

Corresponding Author

Srimanta Pakhira − *Theoretical Condensed Matter Physics and Advanced Computational Materials Science Laboratory, Department of Physics, Indian Institute of Technology Indore (IIT Indore), Indore, Madhya Pradesh 453552, India; Theoretical Condensed Matter Physics and Advanced Computational Materials Science Laboratory, Centre for Advanced Electronics (CAE), Indian Institute of Technology Indore, Indore, Madhya Pradesh 453552, India;* orcid.org/0000-0002-2488-300X; Email: spakhira@iiti.ac.in, spakhirafsu@gmail.com

Author

Dikeshwar Halba − *Theoretical Condensed Matter Physics and Advanced Computational Materials Science Laboratory, Department of Physics, Indian Institute of Technology Indore (IIT Indore), Indore, Madhya Pradesh 453552, India;* orcid.org/0000-0002-5530-674X

Complete contact information is available at: https://pubs.acs.org/10.1021/acsomega.4c03544

Notes

The authors declare no competing financial interest.

■ ACKNOWLEDGMENTS

This work was financially supported by the Science and Engineering Research Board-Department of Science and Technology (SERB-DST), Government of India, under grant no. CRG/2021/000572. Dr Pakhira thanks the SERB-DST for providing the highly prestigious Core Research Grant (CRG), SERB-DST, Govt. of India under the scheme number CRG/2021/000572. Dr Srimanta Pakhira is supported by the IIT Indore, and Mr Dikeshwar Halba thanks the Council of Scientific and Industrial Research (CSIR), Government of India for providing his doctoral fellowship under scheme no. CSIRAWARD/JRF-NET2022/12028. The author acknowledges the SERB-DST for providing computing clusters and programs. We thank the Council of Scientific and Industrial Research (CSIR), Department of Scientific and Industrial Research (DSIR), Ministry of Science and Technology, Government of India for providing the research grant under the scheme no. 22/0883/23/EMR-II. The authors would like to acknowledge the IIT Indore for providing the basic infrastructure to conduct this research work. We thank our institute, IIT Indore, for providing the VASP code to conduct the present research work. The authors express their gratitude to the esteemed reviewers for providing their valuable comments and suggestions.

■ REFERENCES

(1) Khan, K. A.; Hasan, M.; Islam, M. A.; Alim, M. A.; Asma, U.; Hassan, L.; Ali, M. H. A Study on Conventional Energy Sources for Power Production. *Int. J. Adv. Res. Innov. Ideas Educ.* **2018**, *4*, 214−228.

(2) Gray, H. B. Powering the Planet with Solar Fuel. *Nat. Chem.* **2009**, *1*, 7.

(3) Kumar, V.; Pakhira, S. Mechanistic Understanding of Efficient Electrocatalytic Hydrogen Evolution Reaction on 2D Monolayer WSSe Janus Transition Metal Dichalcogenide. *Mol. Syst. Des. Eng.* **2023**, *8*, 1060−1074.

(4) Tyagi, A.; Tripathi, K. M.; Gupta, R. K. Recent Progress in Micro-Scale Energy Storage Devices and Future Aspects. *J. Mater. Chem. A* **2015**, *3*, 22507−22541.

(5) Papiya, F.; Nandy, A.; Mondal, S.; Kundu, P. P. Co/Al_2O_3-RGO Nanocomposite as Cathode Electrocatalyst for Superior Oxygen Reduction in Microbial Fuel Cell Applications: The Effect of Nanocomposite Composition. *Electrochim. Acta* **2017**, *254*, 1−13.

(6) Upadhyay, S. N.; Sardar, V. B.; Singh, A.; Kumar, V.; Pakhira, S. Elucidating the Oxygen Reduction Reaction Mechanism on the Surfaces of 2D Monolayer $CsPbBr_3$ Perovskite. *Phys. Chem. Chem. Phys.* **2022**, *24*, 28283−28294.
(7) Upadhyay, S. N.; Pakhira, S. Nanostructured Pt-Doped 2D $MoSe_2$: An Efficient Bifunctional Electrocatalyst for Both Hydrogen Evolution and Oxygen Reduction Reactions. *Phys. Chem. Chem. Phys.* **2022**, *24*, 22823−22844.
(8) Pakhira, S.; Kumar, V.; Ghosh, S. Revealing the Superior Electrocatalytic Performance of 2D Monolayer WSe_2 Transition Metal Dichalcogenide for Efficient H_2 Evolution Reaction. *Adv. Mater. Interfaces* **2023**, *10*, 2202075.
(9) Zhu, Y.; Lin, Q.; Zhong, Y.; Tahini, H. A.; Shao, Z.; Wang, H. Metal Oxide-Based Materials as an Emerging Family of Hydrogen Evolution Electrocatalysts. *Energy Environ. Sci.* **2020**, *13*, 3361−3392.
(10) Abdelkareem, M. A.; Sayed, E. T.; Nakagawa, N. Significance of Diffusion Layers on the Performance of Liquid and Vapor Feed Passive Direct Methanol Fuel Cells. *Energy* **2020**, *209*, 118492.
(11) Wroblowa, H. S.; Yen-Chi-Pan; Razumney, G. Electroreduction of Oxygen: A New Mechanistic Criterion. *J. Electroanal Chem. Interfacial Electrochem.* **1976**, *69*, 195−201.
(12) Gewirth, A. A.; Thorum, M. S. Electroreduction of Dioxygen for Fuel-Cell Applications: Materials and Challenges. *Inorg. Chem.* **2010**, *49*, 3557−3566.
(13) Khotseng, L. Oxygen Reduction Reaction. *Electrocatal. fuel cells Hydrog. Evol. to Des.* **2018**, *27*, 79098.
(14) Jörissen, L. Bifunctional Oxygen/Air Electrodes. *J. Power Sources* **2006**, *155*, 23−32.
(15) Yuk, S. F.; Cooper, V. R. Tuning Oxygen Electrocatalysis: Via Strain on $LaNiO_3$ (001). *Phys. Chem. Chem. Phys.* **2019**, *21*, 4738−4745.
(16) Abe, Y.; Satoh, I.; Saito, T.; Kan, D.; Shimakawa, Y. Oxygen Reduction Reaction Catalytic Activities of Pure Ni-Based Perovskite-Related Structure Oxides. *Chem. Mater.* **2020**, *32*, 8694−8699.
(17) Zhu, Y.; Liu, D.; Jing, H.; Zhang, F.; Zhang, X.; Hu, S.; Zhang, L.; Wang, J.; Zhang, L.; Zhang, W.; et al. Oxygen Activation on Ba-Containing Perovskite Materials. *Sci. Adv.* **2022**, *8*, 31−34.
(18) Liu, J.; Ma, J.; Zhang, Z.; Qin, Y.; Wang, Y.-J.; Wang, Y.; Tan, R.; Duan, X.; Tian, T. Z.; Zhang, C. H.; et al. others. 2021 Roadmap: Electrocatalysts for Green Catalytic Processes. *J. Phys. Mater.* **2021**, *4*, 022004.
(19) Upadhyay, S. N.; Halba, D.; Yadav, L.; Pakhira, S. Illuminating the Role of Mo Defective 2D Monolayer $MoTe_2$ toward Highly Efficient Electrocatalytic O_2 Reduction Reaction. *Langmuir* **2023**, *39*, 17700−17712.
(20) Gorlin, Y.; Jaramillo, T. F. A Bifunctional Nonprecious Metal Catalyst for Oxygen Reduction and Water Oxidation. *J. Am. Chem. Soc.* **2010**, *132*, 13612−13614.
(21) Lu, Y. C.; Xu, Z.; Gasteiger, H. A.; Chen, S.; Hamad-Schifferli, K.; Shao-Horn, Y. Platinum-Gold Nanoparticles: A Highly Active Bifunctional Electrocatalyst for Rechargeable Lithium-Air Batteries. *J. Am. Chem. Soc.* **2010**, *132*, 12170−12171.
(22) Wang, Y.; Li, Y.; Heine, T. PtTe Monolayer: Two-Dimensional Electrocatalyst with High Basal Plane Activity toward Oxygen Reduction Reaction. *J. Am. Chem. Soc.* **2018**, *140*, 12732−12735.
(23) Meadowcroft, D. B. Low-Cost Oxygen Electrode Material. *Nature* **1970**, *226*, 847−848.
(24) Suntivich, J.; Gasteiger, H. A.; Yabuuchi, N.; Shao-Horn, Y. Electrocatalytic Measurement Methodology of Oxide Catalysts Using a Thin-Film Rotating Disk Electrode. *J. Electrochem. Soc.* **2010**, *157*, B1263.
(25) Roche, I.; Chaînet, E.; Chatenet, M.; Vondrák, J. Carbon-Supported Manganese Oxide Nanoparticles as Electrocatalysts for the Oxygen Reduction Reaction (ORR) in Alkaline Medium: Physical Characterizations and ORR Mechanism. *J. Phys. Chem. C* **2007**, *111*, 1434−1443.
(26) Shao, M.-H.; Sasaki, K.; Adzic, R. R. Pd-Fe Nanoparticles as Electrocatalysts for Oxygen Reduction. *J. Am. Chem. Soc.* **2006**, *128*, 3526−3527.
(27) Suntivich, J.; Gasteiger, H. A.; Yabuuchi, N.; Nakanishi, H.; Goodenough, J. B.; Shao-Horn, Y. Design Principles for Oxygen-Reduction Activity on Perovskite Oxide Catalysts for Fuel Cells and Metal-Air Batteries. *Nat. Chem.* **2011**, *3*, 546−550.
(28) Gao, P.; Grätzel, M.; Nazeeruddin, M. K. Organohalide Lead Perovskites for Photovoltaic Applications. *Energy Environ. Sci.* **2014**, *7*, 2448−2463.
(29) Tan, P.; Liu, M.; Shao, Z.; Ni, M. Recent Advances in Perovskite Oxides as Electrode Materials for Nonaqueous Lithium−Oxygen Batteries. *Adv. Energy Mater.* **2017**, *7*, 1602674.
(30) Beall, C. E.; Fabbri, E.; Schmidt, T. J. Perovskite Oxide Based Electrodes for the Oxygen Reduction and Evolution Reactions: The Underlying Mechanism. *ACS Catal.* **2021**, *11*, 3094−3114.
(31) Bursell, M.; Pirjamali, M.; Kiros, Y. $La_{0.6}Ca_{0.4}CoO_3La_{0.1}Ca_{0.9}MnO_3$ and $LaNiO_3$ as Bifunctional Oxygen Electrodes. *Electrochim. Acta* **2002**, *47*, 1651−1660.
(32) Chen, D.; Chen, C.; Baiyee, Z. M.; Shao, Z.; Ciucci, F. Nonstoichiometric Oxides as Low-Cost and Highly-Efficient Oxygen Reduction/Evolution Catalysts for Low-Temperature Electrochemical Devices. *Chem. Rev.* **2015**, *115*, 9869−9921.
(33) Zhang, D.; Song, Y.; Du, Z.; Wang, L.; Li, Y.; Goodenough, J. B. Active $LaNi_{1-x}Fe_xO_3$ Bifunctional Catalysts for Air Cathodes in Alkaline Media. *J. Mater. Chem. A* **2015**, *3*, 9421−9426.
(34) Liang, H.; Hong, Y.; Zhu, C.; Li, S.; Chen, Y.; Liu, Z.; Ye, D. Influence of Partial Mn-Substitution on Surface Oxygen Species of $LaCoO_3$ Catalysts. *Catal. Today* **2013**, *201*, 98−102.
(35) Da, Y.; Zeng, L.; Wang, C.; Gong, C.; Cui, L. A Simple Approach to Tailor OER Activity of $Sr_xCo_{0.8}Fe_{0.2}O_3$ Perovskite Catalysts. *Electrochim. Acta* **2019**, *300*, 85−92.
(36) Cheriti, M.; Kahoul, A. Double Perovskite Oxides Sr_2MMoO_6 (M = Fe and Co) as Cathode Materials for Oxygen Reduction in Alkaline Medium. *Mater. Res. Bull.* **2012**, *47*, 135−141.
(37) Hong, W. T.; Risch, M.; Stoerzinger, K. A.; Grimaud, A.; Suntivich, J.; Shao-Horn, Y. Toward the Rational Design of Non-Precious Transition Metal Oxides for Oxygen Electrocatalysis. *Energy Environ. Sci.* **2015**, *8*, 1404−1427.
(38) Kresse, G.; Furthmüller, J.; Hafner, J. Theory of the Crystal Structures of Selenium and Tellurium: The Effect of Generalized-Gradient Corrections to the Local-Density Approximation. *Phys. Rev. B* **1994**, *50*, 13181−13185.
(39) Kresse, G.; Furthmüller, J. Efficiency of Ab-Initio Total Energy Calculations for Metals and Semiconductors Using a Plane-Wave Basis Set. *Comput. Mater. Sci.* **1996**, *6*, 15−50.
(40) Perdew, J. P.; Wang, Y. Erratum: Accurate and Simple Analytic Representation of the Electron-Gas Correlation Energy. *Phys. Rev. B* **1992**, *45*, 13244−13249.
(41) Hafner, J. Ab-initio Simulations of Materials Using VASP Density-functional Theory and Beyond. *J. Comput. Chem.* **2008**, *29*, 2044−2078.
(42) Perdew, J. P.; Burke, K.; Ernzerhof, M. Generalized Gradient Approximation Made Simple. *Phys. Rev. Lett.* **1996**, *77*, 3865−3868.
(43) Grimme, S.; Antony, J.; Ehrlich, S.; Krieg, H. A Consistent and Accurate Ab Initio Parametrization of Density Functional Dispersion Correction (DFT-D) for the 94 Elements H-Pu. *J. Chem. Phys.* **2010**, *132*, 154104.
(44) Hu, K.; Wu, M.; Hinokuma, S.; Ohto, T.; Wakisaka, M.; Fujita, J. I.; Ito, Y. Boosting Electrochemical Water Splitting: Via Ternary NiMoCo Hybrid Nanowire Arrays. *J. Mater. Chem. A* **2019**, *7*, 2156−2164.
(45) Momma, K.; Izumi, F. VESTA 3 for Three-Dimensional Visualization of Crystal, Volumetric and Morphology Data. *J. Appl. Crystallogr.* **2011**, *44*, 1272−1276.
(46) Patel, C.; Singh, R.; Dubey, M.; Pandey, S. K.; Upadhyay, S. N.; Kumar, V.; Sriram, S.; Than Htay, M.; Pakhira, S.; Atuchin, V. V.; et al. Large and Uniform Single Crystals of MoS_2 Monolayers for ppb-Level NO_2 Sensing. *ACS Appl. Nano Mater.* **2022**, *5*, 9415−9426.
(47) Singh, A.; Pakhira, S. Unraveling the Electrocatalytic Activity of Platinum Doped Zirconium Disulfide toward the Oxygen Reduction Reaction. *Energy Fuels* **2023**, *37*, 567−579.

https://doi.org/10.1021/acsomega.4c03544
ACS Omega 2024, 9, 35614−35626

(48) Kulkarni, A.; Siahrostami, S.; Patel, A.; Nørskov, J. K. Understanding Catalytic Activity Trends in the Oxygen Reduction Reaction. *Chem. Rev.* **2018**, *118*, 2302−2312.
(49) Yadav, L.; Pakhira, S. Platinum-Adsorbed Defective 2D Monolayer Boron Nitride: A Promising Electrocatalyst for O_2 Reduction Reaction. *J. Mater. Chem. C* **2023**, *11*, 15215−15232.
(50) Guan, L.; Liu, B.; Jin, L.; Guo, J.; Zhao, Q.; Wang, Y.; Fu, G. Electronic Structure and Optical Properties of $LaNiO_3$: First-Principles Calculations. *Solid State Commun.* **2010**, *150*, 2011−2014.
(51) Tang, W.; Sanville, E.; Henkelman, G. A Grid-Based Bader Analysis Algorithm without Lattice Bias. *J. Phys.: Condens. Matter* **2009**, *21*, 084204.
(52) Henkelman, G.; Jónsson, H. Improved Tangent Estimate in the Nudged Elastic Band Method for Finding Minimum Energy Paths and Saddle Points. *J. Chem. Phys.* **2000**, *113*, 9978−9985.
(53) Sheppard, D.; Xiao, P.; Chemelewski, W.; Johnson, D. D.; Henkelman, G. A Generalized Solid-State Nudged Elastic Band Method. *J. Chem. Phys.* **2012**, *136*, 074103.
(54) Das, S.; Bhattacharjee, S.; Mondal, S.; Dutta, S.; Bothra, N.; Pati, S.; Bhattacharyya, S. Bimetallic Zero-Valent Alloy with Measured High-Valent Surface States to Reinforce the Bifunctional Activity in Rechargeable Zinc-Air Batteries. *ACS Sustainable Chem. Eng.* **2021**, *9*, 14868−14880.
(55) Hao, Y.; Gong, P.-L.; Xu, L.-C.; Pu, J.; Wang, L.; Huang, L.-F. Contrasting Oxygen Reduction Reactions on Zero- and One-Dimensional Defects of MoS_2 for Versatile Applications. *ACS Appl. Mater. Interfaces* **2019**, *11*, 46327−46336.
(56) Singh, A.; Pakhira, S. Synergistic Niobium Doped Two-Dimensional Zirconium Diselenide: An Efficient Electrocatalyst for O_2 Reduction Reaction. *ACS Phys. Chem. Au* **2024**, *4*, 40−56.
(57) Singh, A.; Pakhira, S. Revealing the Mechanism and Activity of O_2 Reduction Reaction of Co Nanocluster Encapsulated by Carbon Nanotube. *Energy and Fuels* **2024**, *38* (13), 11837−11851.
(58) Upadhyay, S. N.; Pakhira, S. Mechanism of Electrochemical Oxygen Reduction Reaction at Two-Dimensional Pt-doped $MoSe_2$ Material: An Efficient Electrocatalyst. *J. Mater. Chem. C* **2021**, *9*, 11331−11342.
(59) Niu, W.; Pakhira, S.; Marcus, K.; Li, Z.; Mendoza-Cortes, J. L.; Yang, Y. Apically Dominant Mechanism for Improving Catalytic Activities of N-Doped Carbon Nanotube Arrays in Rechargeable Zinc−Air Battery. *Adv. Energy Mater.* **2018**, *8*, 1800480.
(60) Lei, Y.; Pakhira, S.; Fujisawa, K.; Liu, H.; Guerrero-Bermea, C.; Zhang, T.; Dasgupta, A.; Martinez, L. M.; Singamaneni, S. R.; Wang, K.; et al. Low temperature activation of inert hexagonal boron nitride for metal deposition and single atom catalysis. *MaterialsToday* **2021**, *51*, 108−116.
(61) Hui, J.; Schorr, N. B.; Pakhira, S.; Qu, Z.; Mendoza-Cortes, J. L.; Rodríguez-López, J. Achieving Fast and Efficient K^+ Intercalation on Ultrathin Graphene Electrodes Modified by a Li^+ Based Solid-Electrolyte Interphase. *J. Am. Chem. Soc.* **2018**, *140*, 13599−13603.

https://doi.org/10.1021/acsomega.4c03544
ACS Omega 2024, 9, 35614−35626